

# Disorder Effects on the Quasiparticle and Transport Properties of Two-Dimensional Dirac Fermionic Systems

Bo Fu,<sup>1,2,\*</sup> Yanru Chen,<sup>1,3,\*</sup> Weiwei Chen,<sup>4</sup> Wei Zhu,<sup>4</sup> Ping Cui,<sup>1,3</sup> Qunxiang Li,<sup>1,3,†</sup> Zhenyu Zhang,<sup>1,3,‡</sup> and Qinwei Shi<sup>1</sup>

<sup>1</sup>*International Center for Quantum Design of Functional Materials (ICQD), Hefei National Research Center for Physical Sciences at the Microscale, University of Science and Technology of China, Hefei, Anhui 230026, China*

<sup>2</sup>*School of Sciences, Great Bay University, Dongguan, China*

<sup>3</sup>*Hefei National Laboratory, University of Science and Technology of China, Hefei, Anhui 230088, China*

<sup>4</sup>*Institute of Natural Sciences, Westlake Institute for Advanced Study, 18 Shilongshan Road, Hangzhou 310024, Zhejiang Province, China*

(Dated: August 4, 2023)

Despite extensive existing studies, a complete understanding of the role of disorder in affecting the physical properties of two-dimensional Dirac fermionic systems remains a standing challenge, largely due to obstacles encountered in treating multiple scattering events for such inherently strong scattering systems. Using graphene as an example and a nonperturbative numerical technique, here we reveal that the low energy quasiparticle properties are considerably modified by multiple scattering processes even in the presence of weak scalar potentials. We extract unified power-law energy dependences of the self-energy with fractional exponents from the weak scattering limit to the strong scattering limit from our numerical analysis, leading to sharp reductions of the quasiparticle residues near the Dirac point, eventually vanishing at the Dirac point. The central findings stay valid when the Anderson-type impurities are replaced by correlated Gaussian- or Yukawa-type disorder with varying correlation lengths. The improved understanding gained here also enables us to provide better interpretations of the experimental observations surrounding the temperature and carrier density dependences of the conductivity in ultra-high mobility graphene samples. The approach demonstrated here is expected to find broad applicability in understanding the role of various other types of impurities in two-dimensional Dirac systems.

PACS numbers: 71.23.-k, 72.15.Lh, 72.10.-d, 72.80.Vp

## I. INTRODUCTION

The role of disorder in two-dimensional Dirac fermionic systems [1] was intensively explored in the early 1990's, in part motivated by the observations of localized states in  $d$ -wave superconductivity of cuprate superconductors [2] and plateau transitions in integer quantum Hall effect [3]. In those pioneering studies, it has been shown that even impurities with weak scattering strengths have non-perturbative effects on the quasiparticle properties near the Dirac point [3–5], resulting in intriguing new physical consequences. As an example, an exact conformal field theory was developed to successfully describe the contributions from multiple impurity scattering processes if the nature of weak disorder preserves the continuous chiral symmetry [3–6]. In this scenario, the electron density of states was shown to possess a power-law dependence on energy with fractional exponents, instead of logarithmic behaviors obtained within perturbative treatments [7, 8]. Those findings not only enriched our physical understanding about such disordered systems, but also highlighted the importance of multiple impurity scatter-

ing processes. Nevertheless, the conformal field theory is not applicable to scalar type of impurities that breaks continuous chiral symmetry. In such cases, the elastic scattering time  $\tau$  is short, and the Dirac fermionic systems easily enter into the strong scattering limit (the dimensionless parameter  $E_f\tau/\hbar \leq 1$ ) as the Fermi energy  $E_f$  approaches the Dirac point (here  $E_f$  is measured relative to the Dirac point), calling for new theoretical treatments.

Separately, since the experimental discovery of graphene [9], the past decade has seen a substantial rejuvenation of interest in the study of the role of disorder in two-dimensional Dirac fermionic systems. In particular, graphene serves as an ideal platform for studying disorder effects at or close to the Dirac point, because the system displays linear dispersion over a large energy range. Indeed, extensive unusual transport properties have been reported using ultrahigh-mobility samples [10–19], including that the minimum conductivity at the Dirac point strongly depends on temperature, the conductivity is sublinear in carrier density very close to the Dirac point, and there exists a critical carrier density separating a nonmetallic and a metallic regime characterized by the temperature dependence of resistivity. Such novel transport behaviors not only reflect intriguing physics around the Dirac point in weakly disordered graphene, but potentially also highlight the importance of exotic disorder

\* These authors contributed equally to this work

† Corresponding author. E-mail: liquan@ustc.edu.cn

‡ Corresponding author. E-mail: zhangzy@ustc.edu.cn

effects. To date, those unconventional transport properties of graphene remain to be fully understood, in part because prevailing theoretical treatments have various limitations. For example, the standard Boltzmann transport theory treatments [20–22] only capture subsets of scattering events. Several analytical approaches have also been developed to study the role of disorder in graphene, as exemplified by the functional renormalization-group (fRG) approach [26, 27], but these new developments again only considered the contributions of some subsets of multiple impurity scattering processes and still failed to properly describe the quasiparticle behavior around the Dirac point. Therefore, it is still a standing challenge to reliably treat multi-scattering events in the presence of physically realistic disorder without continuous chiral symmetry. An enabling theoretical approach is needed to include all the multiple scattering events in order to capture the underlying disorder physics, especially near the Dirac point.

In this work, we present numerically exact results of the quasiparticle and transport properties of disordered two-dimensional Dirac fermionic systems as obtained using an accurate momentum-space Lanczos method [28, 29], with disordered graphene around the Dirac point as a concrete example. As shown recently, this method is able to rigorously treat all multiple scattering events from random scalar disorder potentials or other types of impurities. Strikingly, we extract from numerical data a universal power-law functional form of the self-energy in describing the multiple scattering effect of disorder on the quasiparticle behavior, which is valid from the weak to strong scattering limit. The newly established universal power law enables us to further reveal the novel quasiparticle behaviors near the Dirac point, such as the unusual energy dependence of the quasiparticle residue. We are also able to reproduce the experimentally observed conductivity versus the carrier density at different temperatures [10, 12, 14, 16], thereby attesting that a proper account of multiple impurity scattering processes is essential in understanding the transport properties of disordered graphene. The approach demonstrated here is expected to find broad applicability in other disordered systems where multiple impurity scattering events play a decisive role.

This paper is organized as follows. The model and methodologies are introduced in Sec. II, followed by the numerical results for the self-energy and quasiparticle properties in Sec. III. The transport properties are given in Sec. IV. We discuss two kinds of correlated impurity: Gaussian- and Yukawa-type disorder in Sec. V. Finally, in Sec. VI, we draw some conclusions from our main results.

## II. MODEL AND METHOD

In the absence of disorder, graphene can be modeled by a  $\pi$ -band tight-binding Hamiltonian. In our calcula-

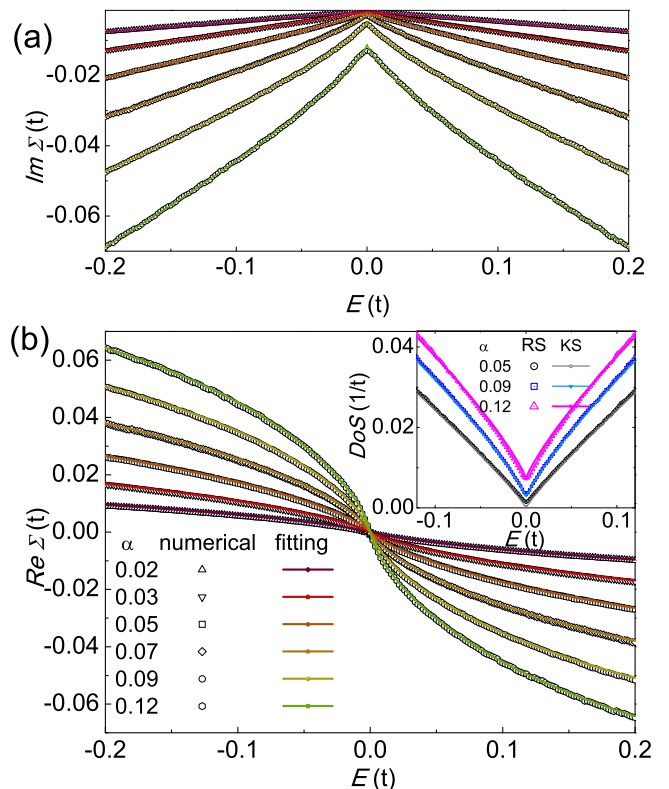


FIG. 1. (a) Imaginary and (b) real parts of the self-energy for disordered graphene with different disorder strengths ( $0.02 \leq \alpha \leq 0.12$ ). The open symbols are the numerical results, while the solid lines are the fitting curves by Eqs. (2) and (3). The inset in (b) shows the comparison of the density of states (DoS) obtained by the real-space Lanczos method (RS, open symbols) with the calculated results based on the fitted self-energy in momentum space (KS, solid lines) for  $\alpha = 0.05, 0.09$ , and  $0.12$ .

tions, the short range Anderson-type disorder is introduced by the on-site energy distributed uniformly and independently within  $[-W/2, W/2]$ . So we consider the following Hamiltonian on a honeycomb lattice:

$$H = t \sum_{\langle ij \rangle} |i\rangle\langle j| + \sum_i V_i |i\rangle\langle i|, \quad (1)$$

where  $t$  is the hopping energy between the nearest neighbouring carbon atoms. A dimensionless parameter  $\alpha = \frac{A_c W^2}{12(\hbar v_f)^2 \pi}$  is defined to characterize the strength of uncorrelated Anderson disorder, where  $A_c = \frac{3\sqrt{3}}{2} a^2$  is the area of the unit cell,  $a$  is the C-C distance, and  $v_f = 3at/2\hbar$  the bare group velocity for clean graphene. To explore the quasiparticle properties of disordered graphene we choose a large graphene sample containing millions of atoms ( $L^2 = 10000^2$ ) to calculate its retarded self-energy ( $\Sigma$ ) by the momentum-space Lanczos recursive method [28, 29]. The large sample in our calculations allows us to choose a small artificial cutoff  $\eta = 0.001$  to simulate the infinitesimal imaginary energy so that we can extract

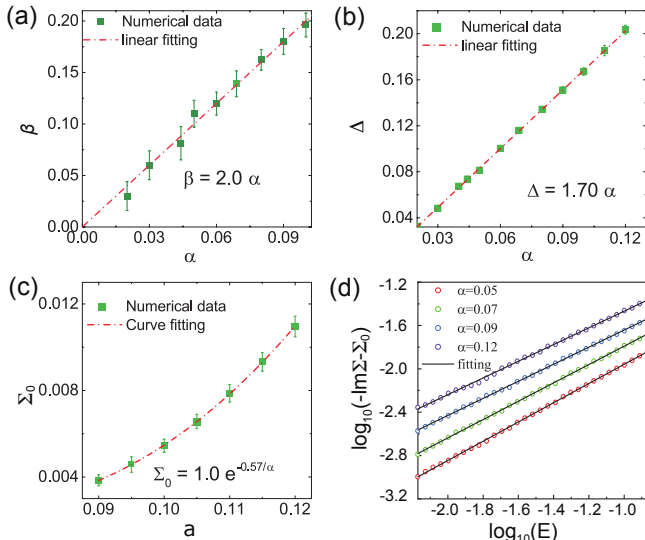


FIG. 2. Numerical fittings of the parameters (a)  $\beta$ , (b)  $\Delta$  and (c)  $\Sigma_0$  as functions of the disorder strength  $\alpha$ .  $\beta$ ,  $\Delta$  and  $\Sigma_0$  are obtained from the power-law self-energy fitting in Fig. 1. (d) Log-log plot of the imaginary part of the self-energy and the power-law fittings by subtracting the values at the zero energy for several disorder strengths.

the self-energy function with high-energy resolution.

### III. SELF-ENERGY AND QUASIPARTICLE PROPERTIES

The imaginary part of the self-energy ( $\text{Im}\Sigma(E)$ ) for disordered graphene with different disorder strengths ( $\alpha$ ) is shown in Fig. 1(a). One can see that, as the disorder strength increases,  $\text{Im}\Sigma(E)$  gradually deviates from a linear behavior, and the absolute value of  $\text{Im}\Sigma(0)$  increases accordingly. These characteristic features inspire us to use a power-law formula to fit our numerical results, given as

$$\text{Im}\Sigma(E) = -\Sigma_0 - \Delta|E|^{1-\beta} \quad 0 < \beta < 1, \quad (2)$$

where  $\beta$ ,  $\Sigma_0$  and  $\Delta$  are the fitting parameters only determined by the disorder strength  $\alpha$ . As shown in Fig. 1(a), the agreement between the self-energy function form in Eq. (2) and numerical results is excellent within the low-energy window of  $[-0.2t, 0.2t]$ . Eq. (2) is further confirmed by the log-log plot of the imaginary part of the self-energy as a function of energy as shown in Fig. 2(d). More remarkably, only via the Kramers-Kronig relation, we identify the functional form of the real part of the self-energy ( $\text{Re}\Sigma(E)$ ) without introducing any other adjustable parameter except the high energy cutoff as

$$\text{Re}\Sigma(E) = D\text{sgn}(E)|E|^{1-\beta} + CE, \quad (3)$$

where  $\text{sgn}(E)$  is the signum function,  $C = \frac{2E_c^{-\beta}}{\pi\beta}\Delta$ , and  $D = -\cot(\frac{\pi}{2}\beta)\Delta$ . The high energy cutoff is chosen as

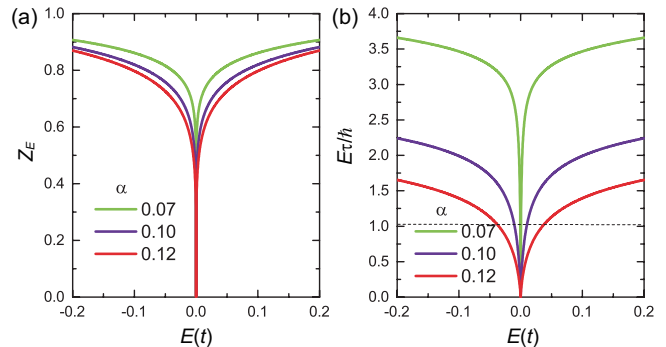


FIG. 3. (a) Quasiparticle residue  $Z_E = v_g/v_f$ ; (b) dimensionless parameter  $E\tau/\hbar$  as a function of  $E$  for different  $\alpha$ .

$E_c \approx 2.7t$ , which has the same order of magnitude of the band width. Such a functional form in Eq. (3) can well fit the numerical results of  $\text{Re}\Sigma(E)$ , as shown in Fig. 1(b). This further confirms the correctness of our proposed power-law formula for the imaginary part of the self-energy. We have also calculated the spectral function as shown in Appendix. A, demonstrating that this power-law relation significantly renormalizes the quasiparticle properties around the Dirac point. Moreover, the inset in Fig. 1(b) plots the comparison of the density of states (DoS) obtained by the widely used Lanczos method in real space [30] with that calculated using our fitted self-energy, showing again the perfect agreement with each other. More discussions about the DoS are given in Appendix. B.

Equations (2) and (3) are the main discoveries of the work [31], reflecting that proper treatments of all orders of multi-scattering events will uncover the novel quasiparticle properties around the Dirac point. More interestingly, the existence of nonzero  $\Sigma_0$  in the obtained self-energy functional form is reminiscent of what is reported in multichannel Kondo problem [32], thereby suggesting that some novel quasiparticle behaviors and unconventional transport properties should be observed even in weakly disordered graphene.

In the following, we digest the central findings in several important physical aspects. First, we discuss the relationship between the fitting parameters and disorder strength. In Fig. 2(a), a linear fitting of  $\beta$  versus  $\alpha \in [0.04, 0.12]$  gives a slope of  $2.00 \pm 0.05$ .  $\Delta$  also has a linear relation with  $\alpha$ , and the fitting slope is  $1.70 \pm 0.05$ , as shown in Fig. 2(b). On the other hand,  $\Sigma_0$  can be fitted by an exponential function  $Ae^{-B/\alpha}$ , and the fitting parameters are  $A = 1.0 \pm 0.1$  in unit of  $t$  and  $B = 0.57 \pm 0.05$ , as shown in Fig. 2(c). Note that the exponential fitting parameter for  $\Sigma_0$  is  $B = 0.57 \pm 0.05$ , which is roughly a factor of 2 off the prediction ( $B=1$ ) within the self-consistent Born approximation (SCBA) [25, 33].

Since all information of the quasiparticle properties is encoded in the self-energy function, next we discuss how the multi-scattering events considerably affect the quasiparticle properties. The real part of the self-energy ( $\text{Re}\Sigma$ )

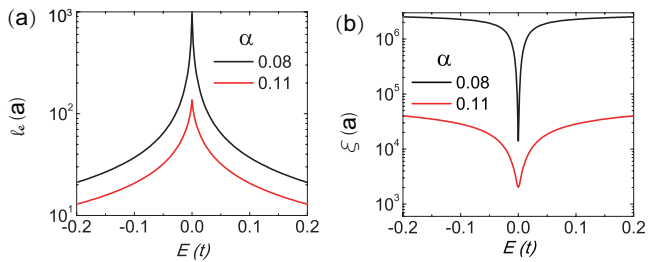


FIG. 4. (a) The mean free path  $\ell_e$  and (b) the localization length  $\xi$  as a function of the energy for disorder strengths  $\alpha = 0.08$  and  $0.11$ .

in Eq.(3) contains two terms, a linear term ( $CE$ ) and a singular one ( $D\text{sgn}(E)|E|^{1-\beta}$ ). We find that the singular term will dominate the quasiparticle behavior around the Dirac point, leading to a super-linear dispersion of  $E_k \propto k^{1/(1-\beta)}$ , where  $E_k$  is the root of  $E - \hbar v_f k - \text{Re}\Sigma(E) = 0$ . This result clearly indicates that the linear dispersion for the ideal graphene is unstable against disorder due to multiple scattering events. Moreover, the power-law correction for the real part of the self-energy leads to the quasiparticle residue  $Z_E = 1/[1 - \partial_E \text{Re}\Sigma(E)] \propto E^\beta$  vanishing as  $E \rightarrow 0$ , so does the effective group velocity  $v_g = \partial E_k / \hbar \partial k = Z_E v_f$ , as shown in Fig. 3(a). In the weak scattering limit ( $E_f \tau / \hbar \gg 1$ ),  $Z_E$  is close to 1.0, and decreases slowly as the Fermi energy decreases. In the strong scattering limit, however,  $Z_E$  (or  $v_g$ ) drops rapidly to zero at the Dirac point. This unusual feature directly demonstrates that multiple scattering events significantly modify the quasiparticle properties near the Dirac point. Therefore, it is naturally expected that unconventional low-energy transport behaviors may arise in disordered graphene.

Indeed, the elastic mean free path  $\ell_e$  is given by the self-energy as  $\ell_e = v_g \tau = 3at / [-4\text{Im}\Sigma(E)]$ , where the elastic mean free time  $\tau$  can be expressed as  $\tau = \hbar / [-2Z_E \text{Im}\Sigma(E)]$ . Using our finding for  $\Sigma_0$ , the mean free path remains finite  $\ell_e(0) \sim a \exp(0.57/\alpha)$  at the Dirac point, which is consistent with the results from the one-loop RG calculations [25, 34]. But the lifetime  $\tau$  diverges as  $\propto E^{-\beta}$  in the limit  $E \rightarrow 0$ , in stark contrast with the Fermi's golden rule prediction ( $\tau \propto E^{-1}$ ), clarifying the significance of the multi-scattering events again. Fig. 3(b) plots the dimensionless parameter ( $E\tau/\hbar$ ) as a function of energy ( $E$ ) in order to point out the low-energy window  $|E| \approx E_c \exp(-1/2\alpha)$ , which corresponds to the strong scattering regime ( $E\tau/\hbar \leq 1$ ). As shown in Fig. 4(a), we plot the energy dependence of  $\ell_e$  for  $\alpha = 0.08$  and  $0.11$ . With the decreasing disorder strength,  $\ell_e$  at the Dirac point becomes longer. According to the scaling theory of Anderson localization, the 2D localization length ( $\xi$ ) can be evaluated exclusively based on the diffusive transport properties  $\xi = 2\ell_e \exp(\pi\sigma_d/G_0)$  (orthogonal symmetry) [35–37], with  $\sigma_d$  the conductivity of the system and  $G_0 = 2e^2/h$ . Fig. 3(d) shows that  $\xi$  depends sensitively on the disorder strength and is strongly

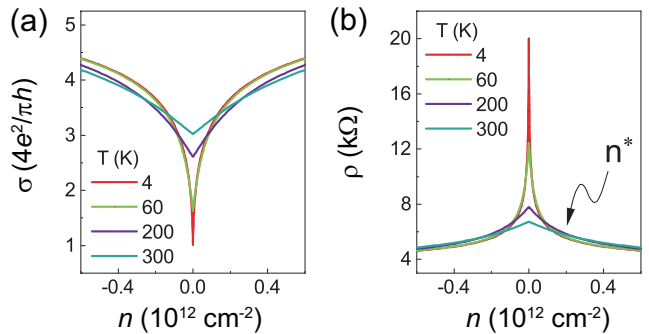


FIG. 5. (a) Conductivity  $\sigma_{xx}$  and (b) resistivity  $\rho$  as functions of the carrier density  $n$  at different temperatures  $T = 4$  K, 60 K, 200 K, and 300 K. The disorder strength is  $\alpha = 0.09$ .

suppressed as  $\alpha$  increases. The energy dependence of  $\xi$  is mainly dominated by  $\sigma_d$ . As a result, the behavior of  $\xi$  shows a minimum value at the Dirac point, exhibiting an opposite trend as  $\ell_e$ . Moreover, the localization length estimated by our numerical results agrees well with that obtained by the transfer matrix method [36].

#### IV. TRANSPORT BEHAVIOR

Based on the above self-energy results, we further investigate the transport properties of disordered graphene. First, we study the conductivity with impurity scattering including the multi-scattering events, and then take account the effect of electron-phonon scattering. At last, we consider the higher order correction in addition to the bare current bubble.

##### A. Conductivity With Impurity Scattering

On the Drude formula level, the conductance is given by  $\sigma = \frac{e^2}{h} g$  with the dimensionless electrical conductance  $g \sim k_F \ell_e$ , where  $k_F$  is the Fermi wave vector and  $\ell_e$  is the mean free path. Using the Fermi energy  $E \sim \hbar v_f k_F$  and mean free path  $\ell_e \sim v_f \tau$ , the dimensionless conductance can be rewritten as  $g \sim E\tau/\hbar$ . The conductance  $g$  is a good measure of disorder and can be used as a parameter to interpolate between the weak scattering regime  $g \gg 1$  and the strong scattering regime  $g \leq 1$ . Previous theoretical studies are mainly restricted to extrinsic or doped graphene wherein the Fermi level is away from the charge neutral Dirac point (or weak scattering regime). The numerically exact results about the self-energies allow us to explore the transport behaviors around the charge neutrality point where the dimensionless conductance is not much larger than 1. To include the non-trivial contribution of the quasiparticle residue, we take more rigorous quantum-mechanical treatments based on the Kubo for-



malism to calculate the Drude conductivity by

$$\sigma_{xx}(T, E_f) = \int dE \left( -\frac{\partial f(E, E_f)}{\partial E} \right) \sigma_d(E), \quad (4)$$

where  $f(E, E_f) = 1/[e^{(E-E_f)/T} + 1]$  is the Fermi-Dirac distribution with  $T$  being the temperature, and  $\sigma_d(E)$  is the zero temperature conductivity given as

$$\sigma_d(E) = \frac{G_0}{\pi} \left[ 1 + \chi(E) \tan^{-1} \chi(E) + \frac{\tan^{-1} \chi(E)}{\chi(E)} \right], \quad (5)$$

with  $G_0 = 2e^2/h$  and  $\chi(E) = [E - \text{Re}\Sigma(E)]/\text{Im}\Sigma(E)$ . After introducing a dimensionless function  $\mathcal{G}(E) = \int_0^E \frac{Z(E')}{Z(E)} \frac{dE'}{E} = \frac{1 - \text{Re}\Sigma(E)/E}{1 - \partial_E \text{Re}\Sigma(E)}$ ,  $\chi(E)$  can be rewritten as  $\chi(E) = \mathcal{G}(E)E\tau/\hbar$ . For a small disorder strength ( $\alpha$  or  $\beta \sim 0$ ), our numerical calculation shows that  $\chi(E)$  can be approximated as  $E\tau/\hbar$ . Thus, the Drude conductivity is only determined by the dimensionless parameter  $E\tau/\hbar$ . The conductivity (Eq. (5)) contains two types of contributions: the first term (unity) in the bracket is the contributions of two Green's functions of the same kind (retarded-retarded or advanced-advanced) whereas the second and third terms come from the contribution of the retarded-advanced sector. In the weak scattering regime ( $E\tau/\hbar \gg 1$ ), the conductivity is dominated by the retarded-advanced term and takes the form  $\sigma_d(E) \simeq \frac{G_0}{2} |\chi(E)|$ , suggesting that weak disorder leads to weak dependence of conductivity on the Fermi energy. Around the Dirac point, however, the sublinear behavior of  $E\tau/\hbar$  as plotted in Fig. 3(b) yields a sublinear power-law energy dependence of the obtained zero-temperature conductivity, in agreement with numerical calculations using the finite-size Kubo formalism [38], but in sharp contrast with the prediction calculated by the Fermi's golden rule [39]. More remarkably, it naturally produces the sharp peak in resistivity at low temperature and the strong temperature dependence of the maximum resistivity, due to the sharp dip of  $E\tau/\hbar$  around the Dirac point as shown in Fig. 3(b). Those novel behaviors have been widely reported in ultrahigh-mobility samples at and near the Dirac point [10–19].

To compare with the experimental transport results of high quality graphene in more detail, in the following quantitative evaluations, a typical weak disorder strength is chosen as  $\alpha = 0.09$  without any other adjustable parameter being used. Fig. 5(a) and 5(b) plot the corresponding conductivity  $\sigma_{xx}$  and resistivity  $\rho = 1/\sigma_{xx}$  as functions of the carrier density  $n$  from the temperature 4 K to 300 K, respectively, where  $n = \int_0^\infty D(E)f(E, E_f)dE + \int_{-\infty}^0 D(E)[1 - f(E, E_f)]dE$ , and  $D(E)$  denotes the density of states. Sharp dips (or peaks) in the conductivity (or resistivity) are observed precisely at the Dirac point at low temperatures. By increasing the temperature, the conductivity very close to the Dirac point has a pronounced increase, showing a strong temperature dependence. Most remarkably, there exists a  $T$ -independent carrier density (roughly

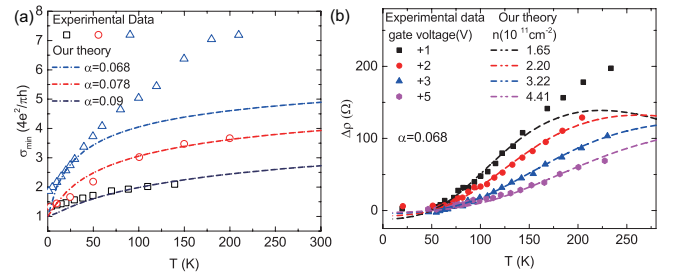


FIG. 6. Comparisons between our theory and the experimental data for the (a) minimum conductivity  $\sigma_{\min}$  and (b) resistivity  $\Delta\rho$  as function of temperature. In (a), the open symbols indicate the temperature dependence of  $\sigma_{\min}$  at the Dirac point for three devices extracted from Ref. [16]. The dashed lines indicates the results according to our theory for three different disorder strengths  $\alpha$ . In (b), the solid symbols represent the temperature dependence of  $\Delta\rho$  for different gate voltages extracted from Ref. [10]. The dash lines are the results according to our theory for different carrier densities.

$n^* \sim 1.5 \times 10^{11} \text{ cm}^{-2}$ ) that divides the systems into two different density regimes. In the low density regime ( $|n| < n^*$ ), the resistivity exhibits a nonmetallic behavior, that is, increasing  $\rho$  for decreasing  $T$ . For  $|n| > n^*$ , the resistivity displays a weak  $T$ -dependence and decreases for decreasing  $T$ .

We separately consider the two density regimes  $|n| < n^*$  and  $|n| > n^*$  and compare our theory with experimental results. We first consider low density regime,  $|n| < n^*$ , and address the  $T$  dependence of the minimum conductivity. Fig. 6(a) shows the comparison of the minimum conductivity  $\sigma_{\min}$  as a function of temperature between our theory and experimental data for three monolayer devices from Ref. [16]. According to our theory,  $\sigma_{\min}$  increases monotonically with  $T$ .  $\sigma_{\min}$  versus  $T$  follows a roughly linear relationship for  $T < 100$  K and becomes sublinear for  $T > 100$  K. The experiment and theory show good agreement for devices  $\square$  and  $\circ$ . For device  $\triangle$ , the theory only fits the experimental data well at low temperature. At finite temperature, electrons in both the conduction band and the valence band can contribute to the electrical conductivity. From Eq.(4), the broadening width of the electron and hole contributions is proportional to the temperature according to the Fermi-Dirac distribution  $f(E, E_f)$ . As the temperature increases, the broadening width also increases, allowing more electron-hole pairs to contribute to the electrical conductivity. The temperature dependence of  $\sigma_{\min}$  depends critically on the transport properties near the Dirac point. We then turn to the high density  $|n| > n^*$ . We depict  $\Delta\rho(T) = \rho(T) - \rho(50 \text{ K})$  as a function of temperature with different carrier densities in Fig. 6(b). The solid dots and dashed lines are experimental data from Ref. [10] and our theory, respectively. In the high temperature range,  $\Delta\rho(T)$  increases nearly linearly with  $T$ . In Ref. [10], the linear temperature dependence is believed to be due to electron-phonon interaction. How-

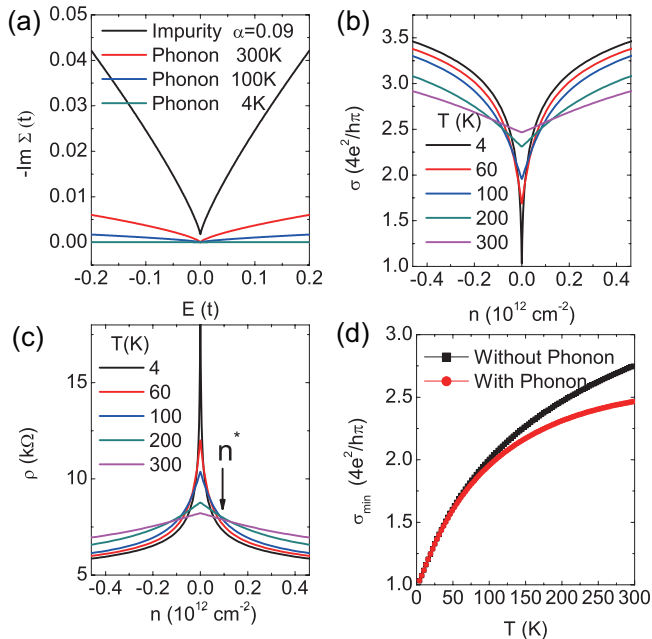


FIG. 7. (a) Imaginary part of the self-energy induced by disorder scattering and phonon scattering at 4 K, 100 K, and 300 K. (b) Conductivity  $\sigma_{xx}$  and (c) resistivity  $\rho$  as functions of the carrier density  $n$  at different temperatures  $T = 4$  K, 60 K, 100 K, 200 K and 300 K including resistive scattering by graphene phonons described by Eq. (6). The disorder strength is  $\alpha = 0.09$ . (d) Comparison of temperature dependence of the minimum conductivity  $\sigma_{\min}$  with and without phonon scattering.

ever, the slope of  $\Delta\rho$  versus  $T$  cannot be explained solely by electron-phonon interaction, as it also depends on the carrier density. Our theory can consistently explain the carrier density and temperature dependence of  $\rho(T)$ . The overall trends of our numerical results are in good agreement with experimental observations [10]. The discrepancy at high temperatures could be due to the neglect of electron-electron scattering and electron-phonon scattering, which become significant at high temperatures. Those findings attest that the strong  $T$ -dependence of the conductivity (resistivity) in the low density regime stems from the multi-scattering effects, which amounts to another important aspect of the present work.

## B. Conductivity With Phonon Scattering

We are now going to take into account the effect of electron-phonon scattering. In graphene, there exists a characteristic wave vector  $q_c$  below which the anharmonic effects become important [40, 41]. It has been estimated that  $q_c = \sqrt{\Delta_c T}/(\hbar v_f) \approx \sqrt{T(K)} \times 0.7 \times 10^8 \text{ m}^{-1}$ , where  $\Delta_c \approx 18.7 \text{ eV}$  [40]. Since our interest is the low carrier density with  $n \leq 0.5 \times 10^{12} \text{ cm}^{-2}$  where the transport properties are strongly influenced by the multiple scattering processes. The Fermi wave vector can be estimated

by  $k_F \approx \sqrt{\pi n} \leq 1.25 \times 10^8 \text{ m}^{-1}$ , and is small compared to  $q_c$  (3.2 K). Therefore, the anharmonic electron-phonon interaction should be taken into account. In this situation, the scattering rate caused by phonon scattering can be expressed as [40]

$$\frac{\hbar}{2\tau(\epsilon)} = \frac{g^2 T^2}{\pi |\epsilon|} C Z^2 \left( \frac{|\epsilon|}{\sqrt{T} \Delta_c} \right)^{2\eta}, \quad (6)$$

where  $g \approx 5.3$  is the dimensionless electron-phonon coupling constant,  $C \approx 2.26$  is an integral coefficient,  $\eta \approx 0.85$  is a critical index [42], and the numerical prefactor  $Z \approx 1$ .

As shown in Fig. 7(a), we compare the magnitude of our calculated imaginary part of the self-energy  $\text{Im}\Sigma$  due to impurity scattering and the contribution arising from the electron-phonon scattering (Eq. (6)) at different temperatures  $T = 4, 100, 300$  K. The disorder strength has been chosen as  $\alpha = 0.09$ . At low temperatures ( $T < 100$  K),  $-\text{Im}\Sigma \gg \frac{\hbar}{2\tau(\epsilon)}$ , and the resistivity of graphene is dominated by scattering of impurities. We also plot the resistivity and conductivity after taking phonon scattering into consideration in Figs. 7(b) and 7(c), and the temperature dependences of the minimum conductivity  $\sigma_{\min}$  with and without phonon scattering are contrasted in Fig. 7(d). By comparing with the results in sec. IV A, we find that our main conclusion would not change even considering the electron-phonon scattering. The crossover carrier density  $n^*$  still exists, separating the regions with the "metallic" (high density) and "insulating" (low density) behaviors.

## C. Higher Order Conductivity Correction

In addition to the bare (zeroth order) current bubble which yields the main contribution to the classical conductivity, the disorder averaging will generate other current bubbles which are expanded in terms of scattering vertices. Two classes of diagrams are usually calculated, the ladder diagram and the maximally-crossed diagrams, which account for the vertex correction and quantum interference correction, respectively.

### 1. Vertex Correction

The Bethe-Salpeter Fermi equations for the vertex correction can be solved by using the single-particle propagators with the full self-energy. With the vertex correction, the Kubo formula for conductivity is given by

$$\begin{aligned} \sigma_{xx}(E) = & -\frac{\hbar e^2 v_f^2}{4\pi} \sum_{ss'=\pm} ss' \int \frac{d^2\mathbf{k}}{(2\pi)^2} \text{Tr}[j_x G(\mathbf{k}, a + i s \eta) \\ & \times J_x(\mathbf{k}, a + i s \eta, a + i s' \eta) G(\mathbf{k}, a + i s' \eta)]. \end{aligned} \quad (7)$$

Here the current vertex  $J_x$  satisfies the following Beta-Salpeter equation [43]:

$$J_x(\mathbf{k}, a + is\eta, a + is'\eta) = j_x + \sum_{\mathbf{k}'} \langle V_{\mathbf{k}-\mathbf{k}'} G(\mathbf{k}', a + is\eta) \times J_x(\mathbf{k}', a + is\eta, a + is'\eta) \times G(\mathbf{k}', E + is'\eta) V_{\mathbf{k}'-\mathbf{k}} \rangle_{\text{dis}}, \quad (8)$$

where we have defined  $E - \text{Re}\Sigma \equiv a$  and  $-\text{Im}\Sigma \equiv \eta$  for simplicity and  $G(\mathbf{k}, a + is\eta) = 1/(a + is\eta - \hbar v_f \mathbf{k} \cdot \boldsymbol{\sigma})$  is the disorder averaged retarded ( $s = +$ ) and advanced ( $s = -$ ) Green's functions with our calculated self-energy. By further assuming that compared with the bare current  $j_x = \sigma_x$ , the renormalized current  $J_x = \Lambda \sigma_x$  only differs by an energy dependent dimensionless coefficient  $\Lambda$ , we can put it into the iterative equation of Eq. (8).

For the short range disorder, after taking inter-valley scattering into account, the vertex correction can be shown to vanish identically due to the symmetry of the first Brillouin zone. Therefore, the vertex correction only contributes in the long range disorder case. As shown in Appendix C, with the vertex correction, the minimum conductivity will be dependent on the disorder strength. For the Fermi energies far from the Dirac point, the vertex correction  $\Lambda = 2$  recovers the result for the weak scattering regime [33, 44]. As one gets close to the Dirac point, the vertex correction becomes negligible due to the sharp reduction near the Dirac point and eventual vanishment at the Dirac point of the quasiparticle residue as plotted in Fig. 3(a).

## 2. Quantum Interference Corrections

Another mystery in graphene transport is the absence of the localization-induced insulating phase in the vicinity of the Dirac point, violating the Ioffe-Regel criterion which states that the electron state will be localized in the region  $E\tau/\hbar \ll 1$  [35, 45]. In undoped samples of graphene, the minimum conductivity is observed to remain almost constant over a wide range of temperatures, from room temperature down to sub-Kelvin temperatures [11, 16]. This behavior is in stark contrast to the well-established results on the conductivity of 2D systems, where localization effects typically drive the system into an insulating state at low temperatures. The absence of localization in graphene is still not fully understood. Our calculations show that the multi-scattering events may provide a plausible mechanism in understanding the absence of the localization. In realistic graphene samples, inter-valley scattering is inevitable, leading to backscattering between the two valleys. As a result, the inter-valley Cooperon channel dominates at small magnetic fields or large sample sizes, leading to weak localization effects and even localization when the quantum interference correction becomes comparable to the classical conductivity. This is the reason why the magnetoresistance in experiments at small magnetic

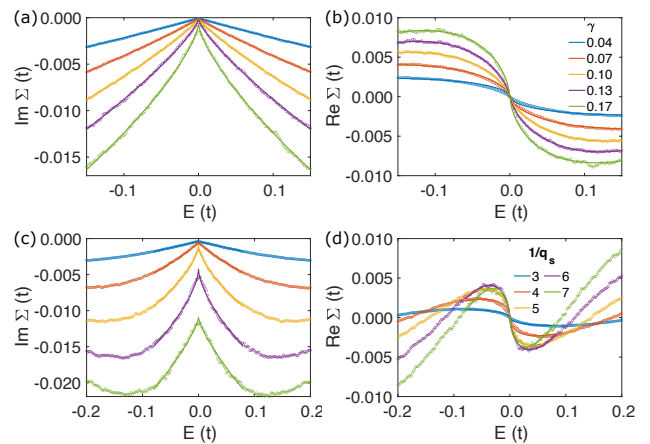


FIG. 8. (a) Imaginary and (b) real parts of the self-energy with a correlated Gaussian potential as a function of energy for different disorder strengths ( $0.04 \leq \gamma \leq 0.17$ ). The circle symbols denote the numerical results obtained from our Lanczos method and the solid lines are the fitting curves. 60 samples are collected for each curve. (c) Imaginary and (d) real parts of the self-energy with Yukawa-type charge impurities as a function of energy for different screening lengths  $1/q_s = 3, 4, 5, 6, 7$  ( $\gamma_c = 0.04, 0.11, 0.22, 0.39, 0.61$ ). The circle symbols denote the numerical results obtained from the Lanczos method and the solid lines are the fitting curves within the energy window  $[-0.08t, 0.08t]$ .

fields is commonly negative, exhibiting a weak localization behavior [46, 47]. Here, we extend the standard calculation from the weak scattering limit [44, 48] to the strong scattering limit to discuss the contribution of the maximally-crossed diagrams by considering the accurate single-particle propagator, shown in Appendix D. In the weak scattering regime, we recover the weak localization correction which arises from the inter-valley scattering induced Cooperon channel [44]. In the strong scattering regime, however, we verify that multi-scattering events will introduce finite Cooperon gaps so that the small momentum singularities in the Cooperon momentum integrals is avoided. Thus, the weak localization correction is strongly suppressed in the vicinity of the Dirac point. This may explain why the Anderson localization is absent in the transport measurements in graphene [11, 12, 16].

## V. CORRELATED IMPURITIES

To simulate various defects in real experimental conditions, we expand our regime of discussions to the cases where each impurity has a finite range. In such cases, two impurities become correlated, and the systems can be characterized as containing correlated potential disorder. Since the correlated potential disorder is smooth at the atomic scale, the inter-valley scattering or backscattering is suppressed. For a correlated potential, the self-energy depends on the energy  $E$  and wave vector  $\mathbf{k}$ , which can be directly obtained by changing the initial state  $|\mathbf{k}\rangle$  in

our numerical method [28]. Here we only focus on the self-energy  $\Sigma(E)$  for  $k = 0$ , which is symmetric about  $E = 0$ . Note that the wavelength of the low-energy quasiparticle approaches infinite in the vicinity of the Dirac point. Therefore, a random potential with a shorter spatial correlated length cannot be seen by the Dirac electronic wave, and it will not influence qualitatively the quasiparticle (self-energy) behaviors. Here we also use the power-law formula [see Eqs. (2) and (3)] to fit the numerical results for the correlated disorder potentials.

### A. Gaussian Potential

First, we consider the most common type, Gaussian correlated disorder potential  $V_i = \sum_{n=1}^{N_{\text{imp}}} \pm u_0 \exp[-|\mathbf{r}_n - \mathbf{r}_i|^2/(2\xi^2)]$ , where  $\xi$  is the Gaussian correlation length. The scatters of  $\pm u_0$  are randomly distributed with equal probability, and  $N_{\text{imp}}$  impurities are randomly located among the  $N = 4000^2$  lattices. We fix the impurity density  $n_{\text{imp}} = N_{\text{imp}}/N = 1\%$  and take  $\xi = 2a$  as an example in the following calculations. After the disorder averages, the disorder potential has a vanishing mean and a smooth form of the correlator:

$$\langle V_i \rangle_{\text{dis}} = 0, \quad (9)$$

$$\langle V_i V_j \rangle_{\text{dis}} = \gamma \frac{(\hbar v_f)^2}{4\pi\xi^2} e^{-|\mathbf{r}_i - \mathbf{r}_j|^2/4\xi^2}, \quad (10)$$

$$\langle V_{\mathbf{k}-\mathbf{k}'} V_{\mathbf{k}'-\mathbf{k}} \rangle_{\text{dis}} = \gamma (\hbar v_f)^2 e^{-\xi^2|\mathbf{k}-\mathbf{k}'|^2}, \quad (11)$$

where  $\gamma = \frac{n_{\text{imp}} u_0^2 (2\pi\xi^2)^2}{A_c (\hbar v_f)^2}$  is the dimensionless disorder strength. As shown in Figs. 8(a) and 8(b), the agreement between the power-law fitting and numerical results obtained for the Lanczos method is very good within the energy window of  $[-0.15t, 0.15t]$ . The linear fittings of  $\beta$  and  $\Delta$  with the disorder strength  $\gamma$  are given in Appendix E, yielding  $\beta = 2.04\gamma$  and  $\Delta = 0.42\gamma$ .

We compare the results of this manuscript with that in the existing literature based on real-space methods and refer to [37], where the momentum relaxation time  $\tau_p(E)$  was investigated. Inverting  $\tau_p(E)$  yields the imaginary part of the self-energy, which can be expressed as  $-\text{Im}\Sigma^R(E) = \hbar/[2\tau_p(E)]$ . We then fit our proposed power-law formula to the data, and as shown in Fig. 9, the formula is a good fit in the low energy regime for  $E \in [-0.15t, 0.15t]$  (equivalently  $[-0.405 \text{ eV}, 0.405 \text{ eV}]$ ).

### B. Yukawa Potential

Considering the observation of electron-hole puddles, we also consider the case of a Yukawa-type potential  $V_i = \sum_{n=1}^{N_{\text{imp}}} \pm \frac{e^2}{\kappa|\mathbf{r}_n - \mathbf{r}_i|} \exp[-q_s|\mathbf{r}_n - \mathbf{r}_i|]$ , with positive and negative charged impurities possessing equal probabilities, where  $e$  is the electron charge,  $r_s = e^2/\hbar v_f = 2.2$  is a constant [49],  $\kappa$  is the background dielectric constant,

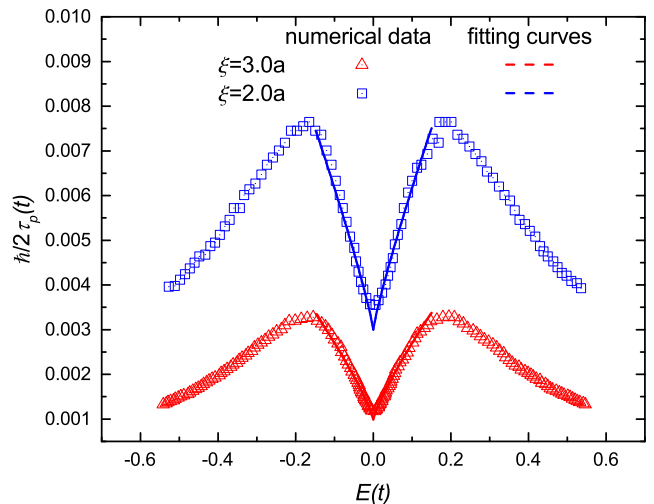


FIG. 9. The fitting of the inverse of the energy-dependent momentum relaxation time  $\tau_p(E)$  by using the power-law formula. The open symbols denote the numerical results extracted from Fig. 16 in Ref.[37] and the dashed lines are the fitting curves.

and  $q_s$  is the inverse screening length. The charge impurities are randomly distributed in the substrate, and we fix the impurity concentration to be  $n_{\text{imp}} = 0.25\%$  ( $\sim 10^{12} \text{ cm}^{-2}$ ) and the distance between the charge and graphene plane to be  $d = 3a$  in the following calculations. By the Fourier transformation, in momentum space, the potential is given by

$$V_q = \frac{V_0}{\sqrt{q_s^2 + q^2}} e^{-d\sqrt{q_s^2 + q^2}}. \quad (12)$$

After averaging the disorder, we obtain

$$\langle V_i \rangle_{\text{dis}} = 0, \quad (13)$$

$$\langle V_{\mathbf{k}-\mathbf{k}'} V_{\mathbf{k}'-\mathbf{k}} \rangle_{\text{dis}} = \frac{n_{\text{imp}}}{A_c} \frac{V_0^2}{q_s^2 + |\mathbf{k}-\mathbf{k}'|^2} e^{-2d\sqrt{q_s^2 + |\mathbf{k}-\mathbf{k}'|^2}}, \quad (14)$$

where  $V_0 = 2\pi e^2/\kappa$ . Here we define the dimensionless disorder strength as  $\gamma_c = \frac{n_{\text{imp}} (2\pi r_s)^2}{A_c \kappa^2 q_s^2} e^{-2q_s d}$ . As shown in Figs. 8(c) and 8(d), the self-energies are given for different screening lengths. In a small energy window, such as  $[-0.08t, 0.08t]$ , the power-law formula can be still used to fit the behavior of the self-energy. At higher energies, this formula does not work because the corresponding Fermi wave vector is larger and the electron wavelengths are comparable to the correlation lengths in this region.

We then compare the results of this manuscript with the existing literature based on real-space methods.

## VI. CONCLUSION

In summary, using the numerically exact momentum-space Lanczos method, we have systematically inves-



tigated the multiple impurity scattering effects on the quasiparticle and transport properties of two-dimensional Dirac fermionic systems in the presence of isolated or correlated weak scalar potentials. We uncover that the multiple impurity scattering processes arising from the weak disorder can induce nontrivial non-Fermi liquid behavior, which is insensitive to the detailed types of disorder. Our theory can account for a set of unconventional findings in the transport measurements: (i) The temperature-dependent resistivity can be divided into two different density regimes: a metallic regime and an insulating regime, separated by  $n^*$ . (ii) For  $|n| < n^*$ , we examined the temperature dependence of the minimum conductivity at the Dirac point. As the temperature increases, the temperature-dependent minimum conductivity first increases linearly, then becomes sublinear, and tends to saturate at higher temperatures. (iii) In the high-density regime  $|n| > n^*$ , the resistivity linearly increases with temperature in the high-temperature range when  $n$  is not too close to  $n^*$ . The slope of the resistivity versus temperature increases as  $n$  gets closer to  $n^*$ . Our theory can consistently explain the temperature and carrier density dependence of conductivity. Our work attests that the vital importance of multiple impurity scattering events in understanding the exotic low energy physics of ultrahigh-mobility graphene.

### ACKNOWLEDGMENTS

We thank Profs. Xin-Cheng Xie, Qing-Feng Sun, and Xiang-Rong Wang for valuable discussions. This work was supported by National Key Research & Development Program of China (No. 2016YFA0200600 and 2017YFA0204904), National Natural Science Foundation of China (No. 21473168, 11634011, 11774325, 12047544, 21603210 and 11974323), Fundamental Research Funds for the Central Universities and the Innovation Program for Quantum Science and Technology (Grant No. 2021ZD0302800). Computational resources are provided by CAS, Shanghai and USTC Supercomputer Centers.

### Appendix A: Spectral Function

To demonstrate how this power-law correction significantly renormalizes the quasiparticle properties around the Dirac point more intuitively, we calculate the spectral function. The single-particle spectral function relates to the Green's function through

$$\begin{aligned}
 A(s\mathbf{k}, E) &= -\frac{1}{\pi} \text{Im}G(s\mathbf{k}, E) \\
 &= \frac{1}{\pi} \frac{-\text{Im}\Sigma}{(E - s\hbar v_f k - \text{Re}\Sigma)^2 + (\text{Im}\Sigma)^2} \quad (\text{A1}) \\
 &= \frac{1}{\pi} \frac{\eta}{(a - s\hbar v_f k)^2 + \eta^2},
 \end{aligned}$$

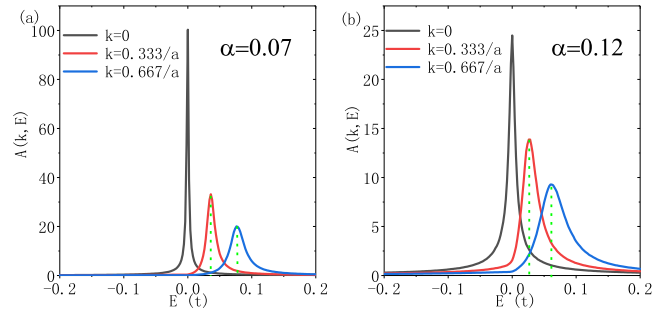


FIG. 10. Single-particle spectral function  $A(\mathbf{k}, E)$  (conduction band) plotted as a function of energy  $E$  at several  $k$  points of  $k = 0.00$  (black lines),  $0.333/a$  (red lines),  $0.666/a$  (blue lines) along the  $k_x$  direction (from left to right). The disorder strength is chosen to be (a)  $\alpha = 0.07$  and (b)  $\alpha = 0.12$ , respectively.

where  $s = \pm$  represents the conduction band and valance band respectively, and we have defined  $E - \text{Re}\Sigma \equiv a$  and  $-\text{Im}\Sigma \equiv \eta$  for simplicity. In the absence of disorder, the spectral function  $A(\mathbf{k}, E)$  is a  $\delta$  function, reflecting that the wave vector  $k$  is a good quantum number and all its weight ratio is precisely at  $E = s\hbar v_f k$ . In the presence of disorder, Eq. (A1) is plotted graphically in Fig. 10. For  $\alpha = 0.07$ ,  $A(\mathbf{k} = 0, E)$  exhibits a sharp peak of a Lorentzian type at  $E = 0$  shown as the black line in Fig. 10(a). When  $k$  moves away from the Dirac point,  $A(\mathbf{k}, E)$  maintains the Lorentzian line shape but becomes much broader due to the increasing of the scattering processes (red and blue lines in Fig. 10(a)). For  $\alpha = 0.12$ ,  $A(\mathbf{k}, E)$  clearly deviates from the Lorentzian type and carries substantially more weight in wings as shown in Fig. 10(b). One can also extract the dispersion relation from the peak of the spectral function  $A(\mathbf{k}, E)$  for a given  $\mathbf{k}$ . The peak of  $A(k = 0.333/a, 0.667/a, E)$  moves toward  $E = 0$  as the disorder strength  $\alpha$  increases, indicating that Dirac electron group velocity  $v_g$  and the dispersion relationship are strongly renormalized due to the multi-scattering events. This is quite different from the usual picture in conventional metal with a finite density of states (DoS), where the life-time effects dominate.

### Appendix B: Density of states

To make our results even more convincing, we revisit the calculation of the DoS based on our spectral function. The single-particle DoS can be easily obtained through our simulated self-energy function as

$$\begin{aligned}
 \rho(E) &= -\frac{A_c}{2\pi} \int \frac{d^2\mathbf{k}}{(2\pi)^2} [\text{Im}G^R(\mathbf{k}+, E) + \text{Im}G^R(\mathbf{k}-, E)] \\
 &= \frac{A_c \eta}{2(\hbar v_f)^2 \pi^2} \left[ \ln \frac{E_c^2}{a^2 + \eta^2} + \frac{2a}{\eta} \tan^{-1} \left( \frac{a}{\eta} \right) \right]. \quad (\text{B1})
 \end{aligned}$$

Here we directly compare this result with the average DoS obtained by the widely used Lanczos method in real space that has been well studied by our former work [50]. As shown in Fig. 1, for a substantial energy range  $[-0.1, 0.1]$ , the DoS calculated by our simulated self-energy agrees well with the results obtained by the real-space method. The line shape of DoS deviates from linearity to sub-linearity as the disorder strength increases, quite similar to the behavior of the imaginary part of the self-energy  $\text{Im}\Sigma(E)$ . Furthermore, according to Eq. (B1) and our simulated results for  $\Sigma_0$  in the main text, the DoS at the Dirac point  $\rho(0) = A_c/(2\hbar^2 v_f^2 \pi^2) \cdot \Sigma_0/\alpha \sim \exp(-1/2\alpha)/\alpha$ , which is also consistent with the results obtained by the functional Renormalization group technique [26, 27].

### Appendix C: Vertex Correction For Conductivity

As mentioned in the main text, the vertex correction only contributes in the long range disorder case. By only considering the intravalley scattering, the current vertex  $J_x$  satisfies the Beta-Salpeter equation of Eq. (8). In the vicinity of the single-valley Dirac point, we can also neglect the momentum-dependence of the disorder potential correlator, and obtain

$$\langle V_{\mathbf{k}-\mathbf{k}'} V_{\mathbf{k}'-\mathbf{k}} \rangle_{\text{dis}} \approx \gamma(\hbar v_f)^2. \quad (\text{C1})$$

Here, we adopt the Gaussian correlated disordered potential that has been described in the main text. The summation of the discrete momentum  $\mathbf{k}$  in Eq. (8) will be replaced by the integral of the first Brillion zone, i.e.,  $1/N \sum_{\mathbf{k}} \rightarrow A_c/(2\pi)^2 \int d^2\mathbf{k}$ , and then

$$\Lambda^{ss'}(E)\sigma_x = \sigma_x + \Lambda^{ss'}(E)\gamma(\hbar v_f)^2 \int \frac{d^2\mathbf{k}'}{(2\pi)^2} \times \frac{1}{a + is\eta - \hbar v_f \mathbf{k}' \cdot \boldsymbol{\sigma}} \sigma_x \frac{1}{a + is'\eta - \hbar v_f \mathbf{k}' \cdot \boldsymbol{\sigma}}. \quad (\text{C2})$$

With some algebraic operation, one can directly obtain

$$\Lambda^{ss'}(E) = [1 - \frac{\gamma}{4\pi} \mathcal{I}(E, s, s')]^{-1}, \quad (\text{C3})$$

with

$$\mathcal{I}(E, s, s') = \int_0^{k_c} dk k \frac{2(\hbar v_f)^2(a + is\eta)}{(a + is\eta)^2 - (\hbar v_f k)^2} \times \frac{(a + is'\eta)}{(a + is'\eta)^2 - (\hbar v_f k)^2}. \quad (\text{C4})$$

After performing the integration, we have

$$\begin{aligned} \mathcal{I}(E, +, +) &= \mathcal{I}(E, -, -) = -1, \\ \mathcal{I}(E, +, -) &= \mathcal{I}(E, -, +) = \left(\frac{a}{\eta} + \frac{\eta}{a}\right) \arctan \frac{a}{\eta}. \end{aligned} \quad (\text{C5})$$

Finally, we find that with the vertex correction, the Kubo formula for conductivity is given by

$$\begin{aligned} \sigma_{xx}(E) &= -\frac{\hbar e^2 v_f^2}{4\pi} \sum_{ss'=\pm} ss' \int \frac{d^2\mathbf{k}}{(2\pi)^2} \text{Tr}[\sigma_x G(\mathbf{k}, a + is\eta) \\ &\quad \times J_x(\mathbf{k}, a + is\eta, a + is'\eta) G(\mathbf{k}, a + is'\eta)] \\ &= \frac{e^2}{2\pi\hbar} \frac{1 + \mathcal{I}(E)}{(1 + \gamma/4\pi)(1 - \gamma/4\pi\mathcal{I}(E))}, \end{aligned} \quad (\text{C6})$$

where  $\mathcal{I}(E) = (a/\eta + \eta/a)\arctan(a/\eta)$ . At  $E = 0$ , we have  $\mathcal{I}(E = 0) = 1$ , and then get

$$\sigma_{xx}(E = 0) = \frac{e^2}{\pi\hbar} \frac{1}{1 - (\frac{\gamma}{4\pi})^2}. \quad (\text{C7})$$

According to Eq. (C7), the minimum conductivity will be dependent on the disorder strength with the vertex correction. However, this dependence is extremely small. As one moves away from the Dirac point, the vertex correction becomes large and gradually gets close to the result  $\Lambda = 2$  in the conventional metal.

### Appendix D: Quantum Interference Corrections For Conductivity

In this section, we calculate the quantum correction to the classical conductivity. The low energy electron excitation of graphene is well described by the two-valley massless Dirac model in two dimension that is given by

$$H_s = \hbar v_f (s k_x \sigma_x - k_y \sigma_y), \quad (\text{D1})$$

where  $s = \pm$  stands for  $K$  and  $K'$  valleys, respectively. We suppose that the Fermi level  $E_f$  intersects the conduction band with the dispersion as

$$\epsilon_{\mathbf{k}} = \hbar v_f |\mathbf{k}|, \quad (\text{D2})$$

and the corresponding eigenfunctions are

$$\langle \mathbf{r} | s\mathbf{k} \rangle = \psi_{s\mathbf{k}}(\mathbf{r}) = \frac{1}{\sqrt{2S}} \begin{bmatrix} 1 \\ s e^{-is\theta_{\mathbf{k}}} \end{bmatrix} e^{i\mathbf{k}\cdot\mathbf{r}}. \quad (\text{D3})$$

The disorder-induced self-energy is obtained numerically through the momentum-space Lanczos methods introduced in the main text, and then the retarded (R) and advanced (A) Green's functions have the form

$$G_{K,K'}^{R/A}(\mathbf{k}, \omega) = \frac{1}{\omega - \epsilon_{\mathbf{k}} - \text{Re}\Sigma^R(\omega) \mp i\text{Im}\Sigma^R(\omega)}. \quad (\text{D4})$$

In order to evaluate the quantum correction to the classical conductivity, we need to calculate a summation of maximally crossed diagrams, which is denoted by

$$\sigma_{qi} = \sigma_{KK}^{KK} + \sigma_{K'K'}^{K'K'} + \sigma_{K'K}^{KK'} + \sigma_{KK'}^{K'K}, \quad (\text{D5})$$

with

$$\sigma_{KK}^{KK} = \frac{e^2 \hbar}{2\pi S} \sum_{\mathbf{k}} \sum_{\mathbf{q}} \Gamma_{KK}^{KK}(\theta_{\mathbf{k}}, \theta_{-\mathbf{k}}, \mathbf{q}) G_K^R(\mathbf{k}) v_K^x(\mathbf{k}) G_K^A(\mathbf{k}) G_K^R(\mathbf{q} - \mathbf{k}) v_K^x(\mathbf{q} - \mathbf{k}) G_K^A(\mathbf{q} - \mathbf{k}), \quad (\text{D6})$$

$$\sigma_{\bar{K}\bar{K}}^{K\bar{K}} = \frac{e^2 \hbar}{2\pi S} \sum_{\mathbf{k}} \sum_{\mathbf{q}} \Gamma_{\bar{K}\bar{K}}^{K\bar{K}}(\mathbf{q}) G_K^R(\mathbf{k}) v_K^x(\mathbf{k}) G_K^A(\mathbf{k}) G_K^R(\mathbf{q} - \mathbf{k}) v_K^x(\mathbf{q} - \mathbf{k}) G_K^A(\mathbf{q} - \mathbf{k}). \quad (\text{D7})$$

There exists three types of Cooperon (particle-particle

type) channels and the full vertex function  $\Gamma$  is related to  $\gamma$  by the Bethe-Salpter equation:

$$\Gamma_{KK}^{KK}(\theta_{\mathbf{p}}, \theta_{\mathbf{p}'}; \mathbf{q}) = \gamma_{KK}^{KK}(\theta_{\mathbf{p}}, \theta_{\mathbf{p}'}) + \frac{1}{S} \sum_{\mathbf{k}} \gamma_{KK}^{KK}(\theta_{\mathbf{p}}, \theta_{\mathbf{k}}) G_K^R(\mathbf{k}) G_K^A(\mathbf{q} - \mathbf{k}) \Gamma_{KK}^{KK}(\theta_{\mathbf{k}}, \theta_{\mathbf{p}'}; \mathbf{q}), \quad (\text{D8})$$

$$\begin{aligned} \Gamma_{\bar{K}\bar{K}}^{KK}(\theta_{\mathbf{p}}, \theta_{\mathbf{p}'}; \mathbf{q}) &= \gamma_{\bar{K}\bar{K}}^{KK}(\theta_{\mathbf{p}}, \theta_{\mathbf{p}'}) + \frac{1}{S} \sum_{\mathbf{k}} \left[ \gamma_{\bar{K}\bar{K}}^{KK}(\theta_{\mathbf{p}}, \theta_{\mathbf{k}}) G_K^R(\mathbf{k}) G_K^A(\mathbf{q} - \mathbf{k}) \Gamma_{\bar{K}\bar{K}}^{KK}(\theta_{\mathbf{k}}, \theta_{\mathbf{p}'}; \mathbf{q}) \right. \\ &\quad \left. + \gamma_{\bar{K}\bar{K}}^{K\bar{K}}(\theta_{\mathbf{p}}, \theta_{\mathbf{k}}) G_K^R(\mathbf{k}) G_K^A(\mathbf{q} - \mathbf{k}) \Gamma_{\bar{K}\bar{K}}^{K\bar{K}}(\theta_{\mathbf{k}}, \theta_{\mathbf{p}'}; \mathbf{q}) \right], \end{aligned} \quad (\text{D9})$$

$$\begin{aligned} \Gamma_{\bar{K}\bar{K}}^{K\bar{K}}(\theta_{\mathbf{p}}, \theta_{\mathbf{p}'}; \mathbf{q}) &= \gamma_{\bar{K}\bar{K}}^{K\bar{K}}(\theta_{\mathbf{p}}, \theta_{\mathbf{p}'}) + \frac{1}{S} \sum_{\mathbf{k}} \left[ \gamma_{\bar{K}\bar{K}}^{KK}(\theta_{\mathbf{p}}, \theta_{\mathbf{k}}) G_K^R(\mathbf{k}) G_K^A(\mathbf{q} - \mathbf{k}) \Gamma_{\bar{K}\bar{K}}^{K\bar{K}}(\theta_{\mathbf{k}}, \theta_{\mathbf{p}'}; \mathbf{q}) \right. \\ &\quad \left. + \gamma_{\bar{K}\bar{K}}^{K\bar{K}}(\theta_{\mathbf{p}}, \theta_{\mathbf{k}}) G_K^R(\mathbf{k}) G_K^A(\mathbf{q} - \mathbf{k}) \Gamma_{\bar{K}\bar{K}}^{K\bar{K}}(\theta_{\mathbf{k}}, \theta_{\mathbf{p}'}; \mathbf{q}) \right]. \end{aligned} \quad (\text{D10})$$

where  $\theta_{\mathbf{p}}$  and  $\theta_{\mathbf{p}'}$  label the incoming and outgoing momenta, respectively, and we have neglected the  $\mathbf{q}$  dependence in the bare scattering vertex. The bare scattering vertex which only causes small momentum transfer within the single valley can be expressed as

$$\begin{aligned} \gamma_{KK}^{KK}(\theta_{\mathbf{p}}, \theta_{\mathbf{p}'}) &= \frac{(\hbar v_f)^2}{E\tau_0/\hbar} \langle K, \mathbf{p} | K, \mathbf{p}' \rangle \langle K, -\mathbf{p} | K, -\mathbf{p}' \rangle \\ &= \frac{(\hbar v_f)^2}{2E\tau_0/\hbar} \left[ \frac{1}{2} e^{-2i(\theta - \theta')} + e^{-i(\theta - \theta')} + \frac{1}{2} \right], \end{aligned} \quad (\text{D11})$$

and

$$\begin{aligned} \gamma_{\bar{K}\bar{K}}^{KK} &= \gamma_{\bar{K}\bar{K}}^{K\bar{K}} \\ &= \frac{(\hbar v_f)^2}{E\tau_0/\hbar} \langle K, \mathbf{p} | K, \mathbf{p}' \rangle \langle K', -\mathbf{p} | K', -\mathbf{p}' \rangle \\ &= \frac{(\hbar v_f)^2}{2E\tau_0/\hbar} \left[ 1 + \frac{1}{2} e^{i(\theta - \theta')} + \frac{1}{2} e^{-i(\theta - \theta')} \right]. \end{aligned} \quad (\text{D12})$$

The bare scattering vertex which causes the scattering of

electrons between two valleys can be expressed as

$$\begin{aligned} \gamma_{K'K}^{K'K} &= \gamma_{K'K}^{K'K} \\ &= \frac{(\hbar v_f)^2}{E\tau_i/\hbar} \langle K, \mathbf{p} | K', \mathbf{p}' \rangle \langle K', -\mathbf{p} | K - \mathbf{p}' \rangle \\ &= \frac{(\hbar v_f)^2}{2E\tau_i/\hbar} \left[ 1 - \frac{1}{2} e^{i(\theta + \theta')} - \frac{1}{2} e^{-i(\theta + \theta')} \right]. \end{aligned} \quad (\text{D13})$$

We have introduced intra- and inter-disorder strengths of  $\frac{(\hbar v_f)^2}{E\tau_0/\hbar}$  and  $\frac{(\hbar v_f)^2}{E\tau_i/\hbar}$ . The total disorder strength is given in terms of  $\tau_0$  and  $\tau_i$ ,

$$\frac{(\hbar v_f)^2}{E\tau_t/\hbar} = \frac{(\hbar v_f)^2}{E\tau_0/\hbar} + \frac{(\hbar v_f)^2}{E\tau_i/\hbar}. \quad (\text{D14})$$

As shown in Eqs. (D8)-(D10), the radial coordinate  $k$  is only contained in the kernel  $\frac{1}{S} \sum_{\mathbf{k}} G_K^R(\mathbf{k}) G_K^A(\mathbf{q} - \mathbf{k})$  and can be evaluated as

$$\begin{aligned} &\int_0^\infty \frac{dk k}{2\pi} G^R(\mathbf{k} + \frac{\mathbf{q}}{2}) G^A(\frac{\mathbf{q}}{2} - \mathbf{k}) \\ &\approx \frac{\Pi(E)}{(\hbar v_f)^2} \left\{ 1 - i(v_g \tau q) \cos \theta - (v_g \tau q)^2 \cos^2 \theta \right\}, \end{aligned} \quad (\text{D15})$$

with  $\Pi(E) = \frac{\chi(E)}{2\pi} \left( \frac{\pi}{2} + \arctan \chi(E) \right)$ .

For later convenience, we introduce the renormalized relaxation time through  $\Pi(E) \equiv E\tau^*/\hbar$ . The angular

coordinate can be done by using the expansion of the full vertex function  $\Gamma$  and the bare vertex  $\gamma$ :

$$\Gamma(\theta_{\mathbf{p}}, \theta_{\mathbf{p}'}; \mathbf{q}) = \frac{(\hbar v_f)^2}{E\tau_t/\hbar} \sum_{n,m} \Gamma_{nm}(\mathbf{q}) e^{i(n\theta_{\mathbf{p}} - m\theta_{\mathbf{p}'})}, \quad (\text{D16})$$

$$\gamma(\theta_{\mathbf{p}}, \theta_{\mathbf{p}'}) = \frac{(\hbar v_f)^2}{E\tau_t/\hbar} \sum_{n,m} \gamma_{nm} e^{i(n\theta_{\mathbf{p}} - m\theta_{\mathbf{p}'})}. \quad (\text{D17})$$

If we further define

$$\begin{aligned} \Phi_{nm} &= \frac{1}{2\pi} \int_0^{2\pi} d\theta e^{i(m-n)\theta} \\ &\times \{1 - i(v_g\tau q) \cos \theta - (v_g\tau q)^2 \cos^2 \theta\}, \end{aligned} \quad (\text{D18})$$

the expansion coefficients in Eqs. (D8)-(D10) can be expressed in the matrix form

$$\begin{aligned} \mathbf{\Gamma}_{KK}^{KK} &= \gamma_{KK}^{KK} + \gamma_{KK}^{KK} \Phi \mathbf{\Gamma}_{KK}^{KK}, \\ \mathbf{\Gamma}_{\bar{K}\bar{K}}^{KK} &= \gamma_{\bar{K}\bar{K}}^{KK} + \gamma_{\bar{K}\bar{K}}^{KK} \Phi \mathbf{\Gamma}_{\bar{K}\bar{K}}^{KK} + \gamma_{\bar{K}\bar{K}}^{K\bar{K}} \Phi \mathbf{\Gamma}_{\bar{K}\bar{K}}^{K\bar{K}}, \\ \mathbf{\Gamma}_{\bar{K}\bar{K}}^{K\bar{K}} &= \gamma_{\bar{K}\bar{K}}^{K\bar{K}} + \gamma_{\bar{K}\bar{K}}^{K\bar{K}} \Phi \mathbf{\Gamma}_{\bar{K}\bar{K}}^{K\bar{K}} + \gamma_{\bar{K}\bar{K}}^{KK} \Phi \mathbf{\Gamma}_{\bar{K}\bar{K}}^{KK}, \end{aligned} \quad (\text{D19})$$

where the bare scattering vertices are

$$\begin{aligned} \gamma_{KK}^{KK} &= \frac{\tau}{\tau_0} \begin{bmatrix} \frac{1}{2} & 0 & 0 \\ 0 & 1 & 0 \\ 0 & 0 & \frac{1}{2} \end{bmatrix}, \\ \gamma_{\bar{K}\bar{K}}^{K\bar{K}} &= \frac{\tau}{\tau_i} \begin{bmatrix} 0 & 0 & -\frac{1}{2} \\ 0 & 1 & 0 \\ -\frac{1}{2} & 0 & 0 \end{bmatrix}, \\ \gamma_{\bar{K}\bar{K}}^{KK} &= \frac{\tau}{\tau_0} \begin{bmatrix} \frac{1}{2} & 0 & 0 \\ 0 & 1 & 0 \\ 0 & 0 & \frac{1}{2} \end{bmatrix}. \end{aligned} \quad (\text{D20})$$

By truncating up to  $q^2$  terms in small  $q$  limit,  $\Phi$  has the form,

$$\Phi = \frac{\tau^*}{\tau_t} \begin{bmatrix} 1 - \frac{1}{2}(v_g\tau)^2 q^2 & -\frac{1}{2}i v_g\tau q_+ & -\frac{1}{4}\ell_e^2 q_+^2 \\ -\frac{1}{2}i v_g\tau q_- & 1 - \frac{1}{2}(v_g\tau)^2 q^2 & -\frac{1}{2}i v_g\tau q_+ \\ -\frac{1}{4}\ell_e^2 q_-^2 & -\frac{1}{2}i v_g\tau q_- & 1 - \frac{1}{2}(v_g\tau)^2 q^2 \end{bmatrix}, \quad (\text{D21})$$

with  $q^2 = q_x^2 + q_y^2$  and  $q_{\pm} = q_x \pm i q_y$ . The two Cooperon channels  $\mathbf{\Gamma}_{\bar{K}\bar{K}}^{KK}$  and  $\mathbf{\Gamma}_{\bar{K}\bar{K}}^{K\bar{K}}$  in Eq. (D19) are coupled together. By introducing the new variables,

$$\begin{aligned} \mathbf{x} &= \gamma_{\bar{K}\bar{K}}^{KK} + \gamma_{\bar{K}\bar{K}}^{K\bar{K}}, \\ \mathbf{y} &= \gamma_{\bar{K}\bar{K}}^{KK} - \gamma_{\bar{K}\bar{K}}^{K\bar{K}}, \\ \mathbf{z} &= \gamma_{KK}^{KK}, \\ \mathbf{X} &= \mathbf{\Gamma}_{\bar{K}\bar{K}}^{KK} + \mathbf{\Gamma}_{\bar{K}\bar{K}}^{K\bar{K}}, \\ \mathbf{Y} &= \mathbf{\Gamma}_{\bar{K}\bar{K}}^{KK} - \mathbf{\Gamma}_{\bar{K}\bar{K}}^{K\bar{K}}, \\ \mathbf{Z} &= \mathbf{\Gamma}_{KK}^{KK}, \end{aligned} \quad (\text{D22})$$

the coupled Bethe-Salpeter equations (Eq. (D19)) are reduced to uncoupled ones and the expansion coefficients

can be easily solved through

$$\begin{aligned} \mathbf{X} &= [\mathbf{1}_{3\times 3} - \mathbf{x}\Phi]^{-1} \mathbf{x}, \\ \mathbf{Y} &= [\mathbf{1}_{3\times 3} - \mathbf{y}\Phi]^{-1} \mathbf{y}, \\ \mathbf{Z} &= [\mathbf{1}_{3\times 3} - \mathbf{z}\Phi]^{-1} \mathbf{z}. \end{aligned} \quad (\text{D24})$$

By retaining the most singular terms, we can solve the above three matrix equations:

$$\begin{aligned} \mathbf{X} &\approx \begin{bmatrix} 0 & 0 & 0 \\ 0 & \frac{1}{g_x + D_{ter}\tau q^2} & 0 \\ 0 & 0 & 0 \end{bmatrix}, \\ \mathbf{Y} &\approx \begin{bmatrix} 0 & 0 & 0 \\ 0 & \frac{1}{g_y + D_{tra}\tau q^2} & 0 \\ 0 & 0 & 0 \end{bmatrix}, \\ \mathbf{Z} &\approx \begin{bmatrix} 0 & 0 & 0 \\ 0 & \frac{1}{g_z + D_{tra}\tau q^2} & 0 \\ 0 & 0 & 0 \end{bmatrix}, \end{aligned} \quad (\text{D25})$$

with the Cooperon gaps

$$\begin{aligned} g_x &= 1 - \frac{\tau^*}{\tau_t}, \\ g_y &= \left(\frac{\tau_t}{\tau_0} - \frac{\tau_t}{\tau_i}\right)^{-1} - \frac{\tau^*}{\tau_t}, \\ g_z &= \frac{\tau_0 - \tau^*}{2\tau_t}, \end{aligned} \quad (\text{D26})$$

and the diffusive constants for the inter- and intra-Cooperon channels

$$\begin{aligned} D_{ter} &= \left[ \left(2\frac{\tau}{\tau^*} - \frac{\tau_t}{\tau_0} + \frac{\tau_t}{\tau_i}\right)^{-1} + \left(2\frac{\tau_t}{\tau^*} - 1\right)^{-1} \right] \frac{v_g^2 \tau}{2}, \\ D_{tra} &= \frac{\tau^*}{\tau_t} \left(1 + \frac{\tau_t}{\tau_i}\right)^{-1} \frac{v_g^2 \tau}{2}. \end{aligned} \quad (\text{D27})$$

Thus, according to Eq. (D23), these Cooperons are evaluated as

$$\mathbf{\Gamma}_{\bar{K}\bar{K}}^{K\bar{K}}(\theta_{\mathbf{p}}, \theta_{\mathbf{p}'}; \mathbf{q}) = \frac{1}{2} \frac{(\hbar v_f)^2}{E\tau_t/\hbar} \left( \frac{1}{g_x + D_{ter}\tau q^2} - \frac{1}{g_y + D_{ter}\tau q^2} \right), \quad (\text{D28})$$

$$\mathbf{\Gamma}_{\bar{K}\bar{K}}^{KK}(\theta_{\mathbf{p}}, \theta_{\mathbf{p}'}; \mathbf{q}) = \frac{1}{2} \frac{(\hbar v_f)^2}{E\tau_t/\hbar} \left( \frac{1}{g_x + D_{ter}\tau q^2} + \frac{1}{g_y + D_{ter}\tau q^2} \right), \quad (\text{D29})$$

$$\mathbf{\Gamma}_{\bar{K}\bar{K}}^{KK}(\theta_{\mathbf{p}}, \theta_{\mathbf{p}'}; \mathbf{q}) = \frac{1}{2} \frac{(\hbar v_f)^2}{E\tau_t/\hbar} \frac{e^{i(\theta_{\mathbf{p}} - \theta_{\mathbf{p}'})}}{g_z + D_{tra}\tau q^2}. \quad (\text{D30})$$

Generally speaking, the total quantum correction is determined by all these four Cooperon channels (the intra-valley Cooperon channels are doubly degenerate). But, we are interested in how the multi-scattering effects will qualitatively renormalize the quantum interference correction to the conductivity. In the following, we only discuss two limiting regimes with two different types of scattering.



## 1. Short range disorder

For short range impurities,  $2\tau_t = \tau_0 = \tau_i$ , and the intra-valley Cooperon channel  $\Gamma_{\bar{K}\bar{K}}^{KK}$  is always fully gapped with its contribution suppressed. In this situa-

tions, we only need to consider the contribution from the inter-valley Cooperon channel  $\Gamma_{\bar{K}\bar{K}}^{K\bar{K}}$ . From Eq. (D7), we first evaluate the bare Hikami box. Since here we consider that the external momentum is zero, the bare Hikami box for the Cooperon channel  $\Gamma_{\bar{K}\bar{K}}^{K\bar{K}}$  vanishes, and the bare Hikami box contribution for the inter-valley Cooperon channel is

$$\begin{aligned} \sigma_{ter}^{qi(0)} &= \frac{e^2 \hbar}{2\pi} \int \frac{d^2 \mathbf{q}}{(2\pi)^2} \int \frac{d^2 \mathbf{k}}{(2\pi)^2} G_{\bar{K}}^R(\mathbf{k}) v_{\bar{K}}^x(\mathbf{k}) G_{\bar{K}}^A(\mathbf{k}) G_{\bar{K}}^R(-\mathbf{k}) v_{\bar{K}}^x(-\mathbf{k}) G_{\bar{K}}^A(-\mathbf{k}) \Gamma_{\bar{K}\bar{K}}^{K\bar{K}}(\theta_{\mathbf{k}}, \theta_{-\mathbf{k}}; \mathbf{q}) \\ &= -\frac{e^2}{2\pi \hbar} \frac{\frac{1}{2\pi} + \Pi(E)}{E\tau_t/\hbar} \ln \frac{D_{ter}\tau/\ell_e^2 + g_x}{D_{ter}\tau/\ell_\phi^2 + g_x}. \end{aligned} \quad (D31)$$

The full correction to the conductivity should take into account the dressed Hikami box contribution. It is reported to have the same order of magnitude of the bare Hikami box and different signs in two-dimensional sys-

tems with large spin-orbital coupling [44].

For the inter-valley Cooperon channels, we need to consider the following dressed Hikami box contribution,

$$\begin{aligned} \sigma_{ter}^{qi(1)} &= 2 \frac{e^2 \hbar}{2\pi} \int \frac{d^2 \mathbf{q}}{(2\pi)^2} \int \frac{d^2 \mathbf{k}}{(2\pi)^2} \int \frac{d^2 \mathbf{p}}{(2\pi)^2} \Gamma_{\bar{K}\bar{K}}^{K\bar{K}}(\theta_{\mathbf{k}}, \theta_{\mathbf{p}}; \mathbf{q}) \langle U_{-\mathbf{k}, \mathbf{p}}^{K\bar{K}} U_{\mathbf{k}, -\mathbf{p}}^{\bar{K}K} \rangle_{\text{imp}} \\ &\quad \times G_{\bar{K}}^R(-\mathbf{k}) G_{\bar{K}}^R(\mathbf{p}) v_{\bar{K}}^x(\mathbf{p}) G_{\bar{K}}^A(\mathbf{p}) G_{\bar{K}}^R(-\mathbf{p}) G_{\bar{K}}^R(\mathbf{k}) v_{\bar{K}}^x(\mathbf{k}) G_{\bar{K}}^A(\mathbf{k}) \\ &= -\frac{e^2}{2\pi \hbar} \frac{(\frac{1}{2\pi} + \Pi(E))^2}{4(E\tau_t/\hbar)(E\tau_i/\hbar)} \ln \frac{D_{ter}\tau/\ell_e^2 + g_x}{D_{ter}\tau/\ell_\phi^2 + g_x}, \end{aligned} \quad (D32)$$

$$\begin{aligned} \sigma_{ter}^{qi(2)} &= 2 \frac{e^2 \hbar}{2\pi} \int \frac{d^2 \mathbf{q}}{(2\pi)^2} \int \frac{d^2 \mathbf{k}}{(2\pi)^2} \int \frac{d^2 \mathbf{p}}{(2\pi)^2} \Gamma_{\bar{K}\bar{K}}^{K\bar{K}}(\theta_{\mathbf{k}}, \theta_{\mathbf{p}}; \mathbf{q}) \langle U_{-\mathbf{k}, \mathbf{p}}^{K\bar{K}} U_{\mathbf{k}, -\mathbf{p}}^{K\bar{K}} \rangle_{\text{imp}} \\ &\quad \times G_{\bar{K}}^R(-\mathbf{k}) G_{\bar{K}}^R(\mathbf{p}) v_{\bar{K}}^x(\mathbf{p}) G_{\bar{K}}^A(\mathbf{p}) G_{\bar{K}}^R(-\mathbf{p}) G_{\bar{K}}^R(\mathbf{k}) v_{\bar{K}}^x(\mathbf{k}) G_{\bar{K}}^A(\mathbf{k}) \\ &= \frac{e^2}{2\pi \hbar} \frac{(\frac{1}{2\pi} + \Pi(\mu))^2}{4(E\tau_t/\hbar)(E\tau_0/\hbar)} \ln \frac{D_{ter}\tau/\ell_e^2 + g_x}{D_{ter}\tau/\ell_\phi^2 + g_x}. \end{aligned} \quad (D33)$$

After collecting all these contributions, we finally obtain the quantum interference correction for the inter-valley Cooperon channel as

$$\begin{aligned} \sigma_{ter}^{qi} &= \sigma_{ter}^{qi(0)} + \sigma_{ter}^{qi(1)} + \sigma_{ter}^{qi(2)} \\ &= -\frac{e^2}{2\pi \hbar} \frac{\frac{1}{2\pi} + \Pi(E)}{E\tau_t/\hbar} \ln \frac{D_{ter}\tau/\ell_e^2 + g_x}{D_{ter}\tau/\ell_\phi^2 + g_x}. \end{aligned} \quad (D34)$$

If the chemical potential is located far from the Dirac node, we have  $\Pi(E) \sim E\tau/\hbar \gg 1$  and the Cooperon gap  $g_x = 1 - \frac{\tau^*}{\tau_t}$  vanishes since  $\tau^* \sim \tau_t$ . The quantum interference conductivity correction is  $\sigma_{ter}^{qi} = -\frac{e^2}{\pi \hbar} \ln \frac{\ell_\phi}{\ell_e}$ , recovering the results of the conventional weak localization regime. When the chemical potential is near the Dirac point (strong scattering regime), due to the finite

Cooperon gap ( $g_x \approx 1$ ), the quantum interference correction is strongly suppressed.

## 2. Long range disorder

For the long range potential disorder ( $\tau_t \approx \tau_0 \ll \tau_i$ ), the inter-valley Cooperon channel  $\Gamma_{\bar{K}\bar{K}}^{K\bar{K}}$  directly vanishes since  $g_x \approx g_y$  and the channel  $\Gamma_{\bar{K}\bar{K}}^{K\bar{K}}$  can also be neglected since it is proportional to the inter-valley scattering strength. Thus, only the intra-valley channel  $\Gamma_{\bar{K}\bar{K}}^{KK}$  will contribute to the quantum interference correction. The bare Hikami box for the intra-valley Cooperon channel can be evaluated as

$$\begin{aligned}\sigma_{tra}^{qi(0)} &= 2 \times \frac{e^2 \hbar}{2\pi} \int \frac{d^2 \mathbf{q}}{(2\pi)^2} \int \frac{d^2 \mathbf{k}}{(2\pi)^2} G_{\mathbf{K}}^R(\mathbf{k}) v_{\mathbf{K}}^x(\mathbf{k}) G_{\mathbf{K}}^A(\mathbf{k}) G_{\mathbf{K}}^R(-\mathbf{k}) v_{\mathbf{K}}^x(-\mathbf{k}) G_{\mathbf{K}}^A(-\mathbf{k}) \Gamma_{KK}^{KK}(\theta_{\mathbf{k}}, \theta_{-\mathbf{k}}; \mathbf{q}) \\ &\approx \frac{e^2}{2\pi \hbar} \frac{\frac{1}{2\pi} + \Pi(\mu)}{E\tau_t/\hbar} \ln \frac{D_{tra}\tau/\ell_e^2 + g_z}{D_{tra}\tau/\ell_\phi^2 + g_z},\end{aligned}\quad (\text{D35})$$

where the prefactor 2 is due to the degeneracy of the intra-valley Cooperon channel. The phase factor  $e^{i(\theta_{\mathbf{k}} - \theta_{-\mathbf{k}})} = -1$  gives an additional minus sign compared

with the inter-valley Cooperon channels (D28) due to the  $\pi$  berry phase. The dressed Hikami box contributions for the intra-valley Cooperon channels are

$$\begin{aligned}\sigma_{tra}^{qi(1)} &= 4 \frac{e^2}{2\pi \hbar} \int \frac{d^2 \mathbf{q}}{(2\pi)^2} \int \frac{d^2 \mathbf{k}}{(2\pi)^2} \int \frac{d^2 \mathbf{p}}{(2\pi)^2} \Gamma_{KK}^{KK}(\theta_{\mathbf{k}}, \theta_{\mathbf{p}}; \mathbf{q}) \langle U_{-\mathbf{k}, \mathbf{p}}^{KK} U_{\mathbf{k}, -\mathbf{p}}^{KK} \rangle_{imp} \\ &\quad \times G_{\mathbf{K}}^R(-\mathbf{k}) G_{\mathbf{K}}^R(\mathbf{p}) v_{\mathbf{K}}^x(\mathbf{p}) G_{\mathbf{K}}^A(\mathbf{p}) G_{\mathbf{K}}^R(-\mathbf{p}) G_{\mathbf{K}}^R(\mathbf{k}) v_{\mathbf{K}}^x(\mathbf{k}) G_{\mathbf{K}}^A(\mathbf{k}) \\ &= -\frac{e^2}{2\pi \hbar} \frac{(\frac{1}{2\pi} + \Pi(E))^2}{2(E\tau_t/\hbar)^2} \ln \frac{D_{tra}\tau/\ell_e^2 + g_z}{D_{tra}\tau/\ell_\phi^2 + g_z}.\end{aligned}\quad (\text{D36})$$

Then, we can obtain the quantum interference correction for the intra-valley Cooperon channel as

$$\begin{aligned}\sigma_{tra}^{qi} &= \sigma_{tra}^{qi(0)} + \sigma_{tra}^{qi(1)} \\ &= \frac{e^2}{2\pi \hbar} \frac{\frac{1}{2\pi} + \Pi(E)}{E\tau_t/\hbar} \left[ 1 - \frac{\frac{1}{2\pi} + \Pi(E)}{2E\tau_t/\hbar} \right] \\ &\quad \times \ln \frac{D_{tra}\tau/\ell_e^2 + g_z}{D_{tra}\tau/\ell_\phi^2 + g_z}.\end{aligned}\quad (\text{D37})$$

In the weak scattering regime ( $E\tau/\hbar \gg 1$ ), the Cooperon gap  $g_z = \frac{1}{2} \left( 1 - \frac{\tau^*}{\tau_t} \right)$  vanishes since  $\tau^* \sim \tau_t$ . In this situation, after including the vertex correction, the quantum interference conductivity correction is  $\sigma_{ter}^{qi} = \frac{2e^2}{\pi \hbar} \ln \frac{\ell_\phi}{\ell_e}$ , recovering the results of the weak anti-localization for the symplectic symmetry class. When the chemical potential is near the Dirac point (strong scattering regime), the Cooperon gap is finite ( $g_z \approx \frac{1}{2}$ ), the quantum interference correction will be strongly suppressed.

#### Appendix E: Linear fittings of $\beta$ and $\Delta$ with the correlated Gaussian potential

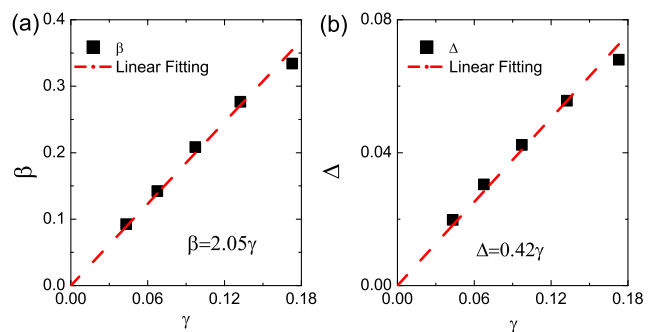


FIG. 11. Linear fittings of (a)  $\beta$  and (b)  $\Delta$  as functions of the disorder strength ( $\gamma$ ) for the correlation length  $\xi = 2.0a$ . The black squares denote the data obtained from the power-law fitting self-energy.

- [1] M. P. A. Fisher and E. Fradkin, Nucl Phys. **B251**, 457 (1985)
- [2] P. A. Lee, Phys. Rev. Lett. **71**, 1887 (1993).
- [3] A. W. W. Ludwig, M. P. Fisher, R. Shankar, G. Grinstein, Phys. Rev. B **50**, 7526 (1994).
- [4] A. A. Nersisyan, A. M. Tselik, F. Wenger, Phys. Rev. Lett. **72**, 2628 (1994).
- [5] C. Mudry, C. de C. Chamon, X. G. Wen, Nucl. Phys. B,

- 466**, 383 (1996).
- [6] B. Sbierski, J. F. Karcher, and M. S. Foster, Phys. Rev. X **10**, 021025 (2020).
- [7] E. Fradkin, Phys. Rev. B **33**, 3257 (1986); *ibid.* **33**, 3263 (1986).
- [8] A. A. Nersisyan, A. M. Tselik, F. Wenger, Nucl. Phys. B. **438**, 561 (1995).
- [9] K. S. Novoselov, A. K. Geim, S. V. Morozov, D. Jiang,

- M. I. Katsnelson, I. V. Grigorieva, S. V. Dubonos, and A. A. Firsov, *Nature* (London). **438**, 197 (2005).
- [10] K. I. Bolotin, K. J. Sikes, J. Hone, H. L. Stormer, P. Kim, *Phys. Rev. Lett.* **101**, 096802 (2008).
- [11] X. Du, I. Skachko, A. Barker, E. Y. Andrei, *Nat. Nanotech.* **3**, 491 (2008).
- [12] L. A. Ponomarenko, A. K. Geim, A. A. Zhukov, R. Jalil, S. V. Morozov, K. S. Novoselov, I. V. Grigorieva, E. H. Hill, V. V. Cheianov, V. I. Fal'ko, K. Watanabe, *Nat. Phys.* **7**, 958 (2011).
- [13] S. V. Morozov, K. S. Novoselov, M. I. Katsnelson, F. Schedin, D. C. Elias, J. A. Jaszczak, and A. K. Geim, *Phys. Rev. Lett.* **100**, 016602 (2008).
- [14] C. R. Dean, A. F. Young, I. Meric, C. Lee, L. Wang, S. Sorgenfrei, K. Watanabe, T. Taniguchi, P. Kim, K. L. Shepard, and J. Hone, *Nat. Nanotechnol.* **5**, 722 (2010).
- [15] P. J. Zomer, S. P. Dash, N. Tombros, and B. J. van Wees, *Appl. Phys. Lett.* **99**, 232104 (2011).
- [16] A. S. Mayorov, D. C. Elias, I. S. Mukhin, S. V. Morozov, L. A. Ponomarenko, K. S. Novoselov, A. K. Geim, and R. V. Gorbachev, *Nano Lett.* **12**, 4629 (2012).
- [17] N. J. G. Couto, D. Costanzo, S. Engels, D. K. Ki, K. Watanabe, T. Taniguchi, C. Stampfer, F. Guinea and A. F. Morpurgo, *Phys. Rev. X*. **4**, 041019 (2014).
- [18] K. R. Amin, S. S. Ray, N. Pal, R. Pandit and A. Bid, *Commun. Phys.* **1**, 1 (2018).
- [19] L. J. Wang, P. Makk, S. Zihlmann, A. Baumgartner, D. I. Indolese, K. Watanabe, T. Taniguchi, and C. Schonenberger, *Phys. Rev. Lett.* **124**, 157701 (2020).
- [20] A. Castro Neto, F. Guinea, N. Peres, K. Novoselov, A. Geim, *Rev. Mod. Phys.* **81**, 109 (2009).
- [21] S. Das Sarma, S. Adam, E. H. Hwang, and E. Rossi, *Rev. Mod. Phys.* **83**, 407 (2011).
- [22] S. Das Sarma and E. H. Hwang, *Phys. Rev. B* **87**, 035415 (2013)
- [23] I. L. Aleiner, K. B. Efetov, *Phys. Rev. Lett.* **97**, 236801 (2006).
- [24] Y. Zheng, T. Ando, *Phys. Rev. B* **65**, 245420 (2002).
- [25] P. M. Ostrovsky, I. V. Gornyi, A. D. Mirlin, *Phys. Rev. B* **74**, 235443 (2006).
- [26] A. Katanin, *Phys. Rev. B* **88**, 241401(R) (2013).
- [27] B. Sbierski, K. A. Madsen, P. W. Brouwer, C. Karrasch, *Phys. Rev. B* **96**, 064203 (2017).
- [28] W. Zhu, Q. W. Shi, X. R. Wang, X. P. Wang, J. L. Yang, J. Chen, J. G. Hou, *Phys. Rev. B* **82**, 153405 (2010).
- [29] B. Fu, W. Zhu, Q. Shi, Q. Li, J. Yang, Z. Zhang, *Phys. Rev. Lett.* **118**, 146401 (2017).
- [30] W. Zhu, Q. Shi, X. Wang, J. Chen, J. Yang, J. Hou, *Phys. Rev. Lett.* **102**, 056803 (2009).
- [31] In general, the self-energy depends on the energy  $E$  and the wavevector  $\vec{k}$ . However our simulation shows that the self-energy is only dependent on the energy.
- [32] A. W. Ludwig, I. Affleck, *Phys. Rev. Lett.* **67**, 3160 (1991).
- [33] T. Ando, *J. Phys. Soc. Jpn.* **75**, 074716 (2006); N. H. Shon and T. Ando, *ibid.* **67**, 2421 (1998).
- [34] A. Schuessler, P. M. Ostrovsky, I. V. Gornyi, A. D. Mirlin, *Phys. Rev. B* **79**, 075405 (2009).
- [35] P. A. Lee, T. V. Ramakrishnan, *Rev. Mod. Phys.* **57**, 287 (1985).
- [36] Z. Fan, A. Uppstu, A. Harju, *Phys. Rev. B* **89**, 245422(2014).
- [37] Z. Fan, J. Garcia, A. Cummings, J. Barrios-Vargas, M. Panhans, A. Harju, F. Ortman, and S. Roche, *Phys. Rep.* **903** 1–69 (2021).
- [38] K. Nomura, A. H. Macdonald, *Phys. Rev. Lett.* **98**, 067702 (2007).
- [39] B. Y.-K. Hu, E. H. Hwang, S. D. Sarma, *Phys. Rev. B* **78**, 165411 (2008).
- [40] I. V. Gornyi, V. Yu. Kachorovskii, and A. D. Mirlin, *Phys. Rev. B* **86**, 165413 (2012).
- [41] E. V. Castro, H. Ochoa, M. I. Katsnelson, R. V. Gorbachev, D. C. Elias, K. S. Novoselov, A. K. Geim, and F. Guinea, *Phys. Rev. Lett.* **105**, 266601 (2010).
- [42] J.-P. Kownacki and D. Mouhanna, *Phys. Rev. E* **79**, 040101(R) (2009).
- [43] N. H. Shon and T. Ando, *J. Phys. Soc. Jpn.* **67**, 2421 (1998).
- [44] E. McCann, K. Kechedzhi, V. I. Fal'ko, H. Suzuura, T. Ando, B. L. Altshuler, *Phys. Rev. Lett.* **97**, 146805 (2006).
- [45] A. F. Ioffe, and A. R. Regel, *Prog. Semicond.* **4**, 237 (1960).
- [46] S. V. Morozov, K. S. Novoselov, M. I. Katsnelson, F. Schedin, L. A. Ponomarenko, D. Jiang, and A. K. Geim *Phys. Rev. Lett.* **97**, 016801 (2006).
- [47] F. V. Tikhonenko, A. A. Kozikov, A. K. Savchenko, and R. V. Gorbachev, *Phys. Rev. Lett.* **103**, 226801 (2009).
- [48] B. Fu, H. -W. Wang, and S.-Q. Shen, *Phys. Rev. Lett.* **122**, 246601 (2019).
- [49] J. P. Reed, B. Uchoa, Y. I. Joe, Y. Gan, D. Casa, E. Fradkin, and P. Abbamonte, *Science* **330**, 805 (2010).
- [50] S. Wu, L. Jing, Q. Li, Q. W. Shi, J. Chen, H. Su, X. Wang, and J. Yang, *Phys. Rev. B* **77**, 195411 (2008).